

High-photon-throughput snapshot colour imaging using a monochromatic digital camera and a pupil-domain diffuser

Jonathan Hauser, Michael A. Golub, Amir Averbuch, Menachem Nathan, Valery A. Zheludev, Omer Inbar & Shay Gurevitch

To cite this article: Jonathan Hauser, Michael A. Golub, Amir Averbuch, Menachem Nathan, Valery A. Zheludev, Omer Inbar & Shay Gurevitch (2019): High-photon-throughput snapshot colour imaging using a monochromatic digital camera and a pupil-domain diffuser, Journal of Modern Optics, DOI: [10.1080/09500340.2019.1567839](https://doi.org/10.1080/09500340.2019.1567839)

To link to this article: <https://doi.org/10.1080/09500340.2019.1567839>



Published online: 24 Jan 2019.



Submit your article to this journal [↗](#)



View Crossmark data [↗](#)



High-photon-throughput snapshot colour imaging using a monochromatic digital camera and a pupil-domain diffuser

Jonathan Hauser^a, Michael A. Golub^a, Amir Averbuch^b, Menachem Nathan^a, Valery A. Zheludev^b, Omer Inbar^a and Shay Gurevitch^a

^aSchool of Electrical Engineering, Faculty of Engineering, Tel Aviv University, Ramat Aviv, Tel Aviv, Israel; ^bSchool of Computer Science, Faculty of Exact Sciences, Tel Aviv University, Ramat Aviv, Tel Aviv, Israel

ABSTRACT

Colour RGB imaging with high throughput was achieved by a monochromatic digital camera with a dispersive diffuser at its pupil. An acquired snapshot monochromatic image was converted to colour coordinates through spectra, by resorting to digital processing with a compressed sensing-based algorithm of spectral imaging. Results of optical evaluation and calibration of an optical system and colour imaging experiments are reported.

ARTICLE HISTORY

Received 10 April 2018
Accepted 2 January 2019

KEYWORDS

Colour and spectral imaging;
image reconstruction

1. Introduction

Existing red–green–blue (RGB) imaging and photographic methods are based on an additive colour model of machine representation of three primary colours from spectral data in the visible range. A straightforward approach for the electro-optical implementation of colour vision is based on time-sequential colour filtering that resorts either to a set of mechanically exchangeable colour filters (1–4) or to an electronically tuneable colour filter, e.g. a liquid crystal filter (5) or Fabry–Perot interferometer (6). However, time-sequential colour filtering is not applicable to single snapshot photography of dynamic fast changing objects. Furthermore, each of the three RGB colour filters transmits about one-third of the incident light flux, while the other two-thirds of light are absorbed, causing substantial light flux losses. The widely used Bayer RGB colour filter array (CFA) (7) includes a spatial pattern of a periodically repeating pattern of one red, two green and one blue filters facing pixels at the image sensor, as shown in Figure 1(a). The Bayer CFA enables snapshot digital colour imaging, but leads to resolution loss and inherits the substantial light flux losses of time-sequential colour filters. While resolution loss in redundant optical images is customarily compensated by an interpolation process called ‘demosaicing’, the lower than 40% light throughput remains an intrinsic disadvantage of the RGB CFA. The white-RGB (WRGB) CFA (8), in which one of the green filters in the Bayer pattern is

replaced with a ‘white’ (transparent or ‘monochromatic’) one, as shown in Figure 1(b), increases light throughput only up to 50%. Furthermore, colour reconstruction in WRGB is sensitive to noise. Some improvement in light throughput can be achieved by resorting to a limited number of RGB pixels at a sparse set of locations on the image sensor with mostly ‘white’ pixels (9), albeit at the expense of colour rendering quality reduction between the sparse RGB pixels. In an alternative approach with a Foveon array (10), each pixel of the image sensor consists of 3 stacked layers of photodetectors, where the top layer is sensitive to blue light, the middle layer is sensitive to green light and the bottom layer is sensitive to red light. While delivering the snapshot mode at full spatial resolution, the Foveon array still suffers from unacceptable losses in light flux at the layers of the image sensor. Another off-the-shelf architecture for RGB imaging which does not include a Bayer CFA is suggested by JAI’s Apex series (11), by performing separate imaging to each colour band using prisms, dichroic filters and multiple sensors. This architecture suggests improved spatial resolution and shows less optical losses compared to a conventional Bayer CFA; however, it includes a quite complicated optical layout.

The quest for an ultimate increase in light throughput led us to the idea of removing all absorbing colour filters and rely on a ‘monochromatic’ image sensor that senses the entire light spectrum at each ‘white’ spatial

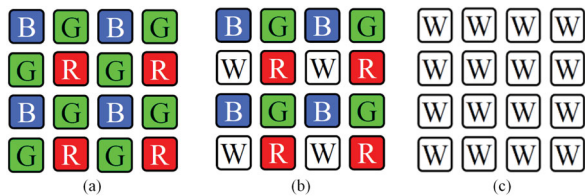


Figure 1. (a) Bayer RGB pattern; (b) WRGB pattern; (c) ‘monochromatic’ sensor pattern, without colour filters.

pixel. We note that colour components can be routinely computed from the full spectrum at each spatial pixel of the image. Past studies report on ‘spectral imaging’ (SI) (12–17), ‘snapshot spectral imaging’ (SSI) (18–22) and Compressive Sensing (CS) (23–28) for the instantaneous (in a single ‘shot’) acquisition of the spectral cube with spatial and spectral data of the object. Recently, several studies have addressed the problem of high-throughput multispectral and colour imaging using a phase element and image reconstruction algorithms. In (29) Wang and Menon present a method for colour imaging (and potentially also spectral imaging) using a transparent diffractive filter array (DFA) which is close to the sensor plane. The suggested system does not include an imaging lens, and the object is placed as close as possible to the DFA. In (30), Wang and Menon generalize the concept presented in (29) by adding an imaging lens in front of the DFA. The lens enabled to increase the field of view and resolution of the reconstructed image, as well as enrich spectral imaging capabilities. In both cases, characterization of the system’s point spread function (PSF) is used to reconstruct the optical flux from the coded sensor measurement. A similar concept is presented in (31), where a method for multispectral and colour imaging using an optical diffuser and without an imaging lens is presented. Here, the diffuser creates a random speckle pattern, which is characterized and used for RGB image recovery using deconvolution.

The system suggested in this paper performs high optical throughput colour imaging, using a pupil-domain, phase-only optical diffuser and a monochromatic sensor. This approach has the potential to cover a larger field of view with respect to lens-less architectures (29, 31). In addition, our method does not involve the assembly of any optical element in proximity of the monochromatic sensor like in (29, 30), thus enabling easier alignment and assembly procedures. Computational spectral-wise colour imaging is performed with the aid of a regular ‘monochromatic’ image sensor (without any colour filters) and without colour filters of any kind in the optical path between an imaged object and the image sensor. Our method resorts to an intermediate stage of snapshot spectral imaging followed by digital computing

of colour coordinates or tri-stimulus values from the spectral cube. Section 2 describes a design of the optical imaging system that forms a diffused and dispersed (DD) image instead of a sharply focused image on the image sensor, to enable well posed computational reconstruction of the colour components through the full spectrum at each spatial pixel. To achieve this, we installed a specially tailored optically transparent dispersive phase-only static diffuser (or simply ‘diffuser’) at the entrance pupil of the imaging lens. We note that this paper is a continuation for the work (27) which proposed a snapshot spectral imaging method for reconstruction of both spatial and entire spectral data of the scene using CS algorithms, in the visible range of wavelength spectrum. In particular, Golub et al. (27) discussed the mathematical model of the diffuser and provided the transition between the continuous optical model and the discrete mathematical model of the optical system. In this paper, we put an emphasis on RGB imaging rather than on acquiring entire spectra. We report higher quality RGB image reconstruction based on an improved optical calibration procedure and adaptation of the CS reconstruction algorithms for the purpose of RGB imaging. Section 3 describes the procedure for optical evaluation and calibration of the spectral-based colour imaging optical system, to define its ‘sensing’ matrix for spatial and spectral image data. Section 4 is dedicated to tailored CS algorithms for digital processing of the DD image recorded on the monochromatic image sensor, to reconstruct the full spectral cube and colour components of the image. Section 5 describes optical experiments for spectral-based colour imaging based on our method. Section 6 reports on experimental investigation for power losses in our method in comparison with a regular Bayer RGB CFA camera. Section 7 provides discussion of results, conclusions and milestones for future research in the field.

2. Model of the optical system with a monochromatic sensor and diffuser

A schematic layout of the spectral-based colour imaging system with a monochromatic image sensor is shown in Figure 2. The colour image is obtained through an intermediate stage of snapshot spectral imaging described in (27). In more detail, the system in Figure 2 includes an imaging lens, a wide bandpass spectral filter, the transmissive phase-only diffuser at the ‘pupil domain’, i.e. at the entrance pupil or at the system aperture of the imaging lens, a monochromatic image sensor and a digital processor with blocks for spectral cube reconstruction and conversion to colour data. The stages of the spectral-based colour imaging in our research are as follows:

- Execute optical calibration to find the sensing matrix of the transformation of the objects' spectral cube to the DD image.
- Optically create a single DD image on the monochromatic image sensor.
- Digitally reconstruct the spectral cube of the object from the DD image, using iterative CS-based algorithms (27) for SSI.
- Digitally convert the reconstructed spectral cube into RGB components.

This section presents a set of mathematical equations based on (27) and adapted to current notations. First, Equation (1) describes the complex pupil function of the optical system with the diffuser. Equations (2)–(4) describe the calculation of the PSF and the continuous convolution integral as the monochromatic response of the optical system comprising the diffuser. Spatial and spectral sampling are presented in Equations (5)–(8). Formation of a polychromatic DD image on the monochromatic image sensor is described by Equation (9). The latter enables the matrix formulation of Equations (10)–(12) in terms of the sensing matrix model of the optical system.

In the diffuser design, we resorted to a combination of approaches that are customary in CS theory and classical spectroscopy. Specifically, for successful deconvolution, modern CS theory requires a highly randomized system response with a tailored image blur, whereas classical spectroscopic systems comprise a dispersive optical element like a prism or a diffraction grating. Our single tailored phase diffuser provides wavelength-dependent light diffusion for randomization and serves also as an inherent disperser (27). For characterization of the diffuser, we use Cartesian coordinates u' , v' at the exit pupil, which has aperture dimensions $D_{u'} \times D_{v'}$. Even though the diffuser is located at the entrance pupil of the imaging lens, we resort here to the exit pupil coordinates u' , v' , because other pupil-domain coordinates may be

brought to u' , v' by scaling with the pupil magnification coefficients. Specifically, the diffuser was designed as a set of phase diffractive grooves (27) to provide a one-dimensional (1D) random phase function $\varphi(u'; \lambda_{des})$ at a design wavelength λ_{des} , as shown in an inset in Figure 2. At an arbitrary wavelength, the diffuser exhibits chromatic dispersion and provides a wavelength-dependent pupil function (27)

$$P(u'; \lambda) = \exp \left[i\varphi(u'; \lambda_{des}) \frac{\lambda_{des}}{\lambda} \frac{n(\lambda) - 1}{n(\lambda_{des}) - 1} \right], \quad (1)$$

within $|u'| \leq 0.5 * D_{u'}$, $|v'| \leq 0.5 * D_{v'}$, where $\exp[\cdot]$ denotes the natural exponential function, i denotes the unit imaginary number and $n(\lambda)$ is the refractive index of a transparent material of the diffuser grooves for the wavelength λ . We assumed that before the introduction of the 1D diffuser, optical resolution of the spatially shift invariant imaging system was matched to the pixel pitch of the image sensor. Accordingly, the coherent PSF of the entire imaging system can be calculated as the PSF of the diffuser, i.e. as the inverse Fourier transform of the pupil function, which can be reduced in our case to the 1D version

$$h(x'; \lambda) = \int_{-0.5 * D_{u'}}^{0.5 * D_{u'}} P(\lambda R v_{u'}; \lambda) \exp(i2\pi v_{u'} x') dv_{u'}, \quad (2)$$

where x' is the horizontal coordinate on the image plane, $v_{u'} = u'/\lambda R$ and R is the distance from the centre of the exit pupil to the centre of the image sensor. The intensity $I'(x', y; \lambda)$ contributing to the DD image and calculated separately at single wavelength λ at each vertical coordinate y of the object may be expressed by just a 1D convolution along the horizontal coordinate x of the object

$$I'(x', y; \lambda) = \int h_I(x' - x; \lambda) I(x, y; \lambda) dx, \quad (3)$$

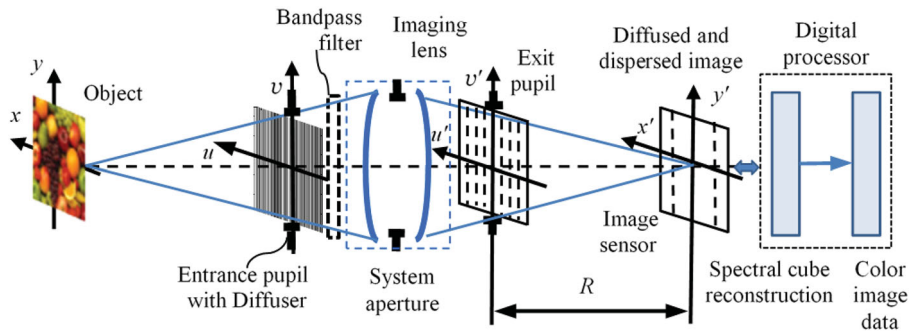


Figure 2. Colour imaging system with monochromatic image sensor, a pupil-domain diffuser and a digital processor for compressed sensing image reconstruction.

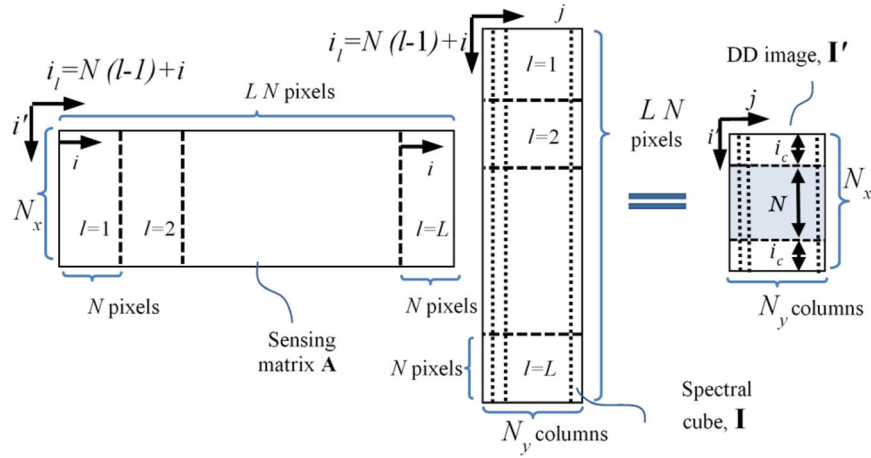


Figure 3. Transformation of the spectral cube to the DD image. **A** is the sensing matrix directly related to the PSF.

of the ideal ('non-dispersed') image $I(x, y; \lambda)$ (i.e. the object in scale of the image) with the incoherent PSF

$$h_I(x'; \lambda) = |h(x'; \lambda)|^2, \quad (4)$$

where $|\cdot|$ denotes the complex absolute value. Mathematical formulations for the digital image processing obviously require a transfer from continuous coordinates and wavelengths to discrete indices of vectors and matrices. Figure 3 shows the mathematical matrix model for the transformation of the spectral cube to the DD image. To define spatial sampling, we consider the discrete pixelated structure of the image sensor, which is characterized, along x and y axes, by a two-dimensional (2D) spatial pitch $\delta_x \times \delta_y$, a number N_x, N_y of pixels, and a number N_b of bits per pixel. The imaging zoom has to match the extension of a blur that is caused by the PSF of the diffuser, such that the entire DD image stays within the aperture of the image sensor, i.e. within N_x pixels in each row and N_y pixels in each column. The 'non-diffused-non-dispersed' image obtained without a diffuser at same zoom is less spread, and occupies accordingly only a smaller number $N < N_x$ of pixels located in the central part of each image sensor row, with margins $i_c = (N_x - N)/2$ on both sides. In the wavelength direction, the spectral cube is also sampled to a finite number L of spectral bands with central wavelengths λ_l , $l = \overline{1, L}$. Throughout this paper, we use the notation $m = \overline{1, M}$ to specify that the value of m may be any natural number between 1 and M . The discrete version of the spectral cube voxels $I_{i,l}^{(j)} = I(x_{i+i_c}, y_j; \lambda_l)$, can be expressed as

$$\mathbf{I} = (I_{i,l}^{(j)}, i = \overline{1, N}, j = \overline{1, N_y}, l = \overline{1, L}), \quad (5)$$

with concatenated spectral and x -spatial dimensions, as shown in Figure 3. In particular, the indices i, j refer to

a column and row pixels coordinates, respectively, in the 'non-diffused-non-dispersed' image on the sensor plane, and the index l refers to the wavelength index.

The discrete versions of $I'(x', y; \lambda)$ and PSF $h_I(x' - x; \lambda)$ are

$$I'_{i',l}^{(j)} = I'(x_{i'}, y_j; \lambda_l) \delta_x, \quad (6)$$

$$\begin{aligned} h_{i'-i,l} &= h_I(x_{i'} - x_{i+i_c}; \lambda_l) \\ &= h_I[(i' - i - i_c) \delta_x - x_{i+i_c}; \lambda_l], \end{aligned} \quad (7)$$

where λ_l refers to the wavelength of index l and i' refers to a column pixel coordinate in the 'diffused and dispersed' image on the sensor plane. Now the continuous 1D convolution in Equation (3) can be approximated by a discrete 1D aperiodic convolution applied separately to each of the N_y image rows $j = \overline{1, N_y}$, and single wavelength band l

$$I'_{i',l}^{(j)} = \sum_{i=1}^N h_{i'-i,l} I_{i,l}^{(j)}. \quad (8)$$

The contribution of the entire set of the wavelength bands $l = \overline{1, L}$ to pixels of the DD image and can be expressed as a weighted sum of the intensities of $I'_{i',l}^{(j)}$, applied through all the wavelength bands

$$I'_{i'}^{(j)} = \sum_{l=1}^L \kappa_l I'_{i',l}^{(j)} = \sum_{l=1}^L \sum_{i=1}^N A_{i',i,l} I_{i,l}^{(j)}, \quad A_{i',i,l} = \kappa_l h_{i'-i,l}, \quad (9)$$

where $\sum_{l=1}^L \cdot$ and $\sum_{i=1}^N \cdot$ denote the sum operators over wavelength and pixel column coordinates, respectively, the non-negative numbers κ_l characterize the overall relative spectral sensitivity of the image sensor and the optical transmission of the optical components of the system for the wavelength λ_l . Note that $A_{i',i,l}$ provide elements of the sensing matrix and, in our model, do not depend on

index $j = \overline{1, N_y}$. Therefore, rows of the object are imaged independently of each other, in match with Equations (3) and (8). Accordingly, each row of the DD image is in one-to-one correspondence with a respective row of the spectral cube. For further data processing, Equation (9) can be expressed in the matrix form

$$\mathbf{A}\mathbf{I} = \mathbf{I}', \quad (10)$$

where \mathbf{I} is the $NL \times N_y$ matrix form of the spectral cube,

$$\mathbf{I}' = [I_{i'}^{(j)}], i' = \overline{1, N_x}, j = \overline{1, N_y}, \quad (11)$$

is the $N_x \times N_y$ matrix representing the DD image, and

$$\mathbf{A} = (A_{i',i,l}), i' = \overline{1, N_x}, i = \overline{1, N}, l = \overline{1, L}, \quad (12)$$

is $N_x \times NL$ block Toeplitz ‘sensing’ matrix, as shown in Figure 3. Note that \mathbf{A} has fewer rows than columns and operates on the spectral cube to form the DD image.

3. Determination of the sensing matrix by system evaluation and calibration

The sensing matrix \mathbf{A} can be directly accessed by system evaluation and calibration procedures, e.g. by direct PSF measurements. This section describes the spatial and spectral calibration procedures that further develop and improve results of (27). In the system shown in Figure 2,

we used an iPad screen as an object in some of the calibration measurements, and in addition, a set of $L = 33$ narrow bandpass spectral filters with 10 nm full-width at half maximum (FWHM) by Thorlabs that covered the 400–720 nm wavelength range in equal gaps of 10 nm. We also used a commercial Ocean Optics USB4000-VIS-NIR calibrated spectrometer.

To prepare for spectral calibration measurements, we considered the nominal spectral transmittance of the narrow 10 nm FWHM bandpass filters, as shown in Figure 4(a), and also a measured one, which was accessed with the spectrometer whose fibre input port was placed first before and then after the bandpass filters. We also averaged the spectral transmittance to an array $[M_l, l = \overline{1, L}]$ with the 10 nm resolution, as shown in Figure 4(b). The nominal and measured arrays are in a pretty good match, except for the 430 and 510 nm bands which are related to some degradation in the quality of these filters over time. At this stage, we neglected spectral cross-talk caused by spectral overlaps between bandpass filters.

To characterize the relative spectral sensitivity κ_l of the optical system in each wavelength band $l = \overline{1, L}$, we resorted to a spatially uniform white patch object on the iPad screen and measured the image spectrum in two ways: first with the spectrometer whose fibre input port was placed after the bandpass filter, and then by sensing the image in the optical system of Figure 2,

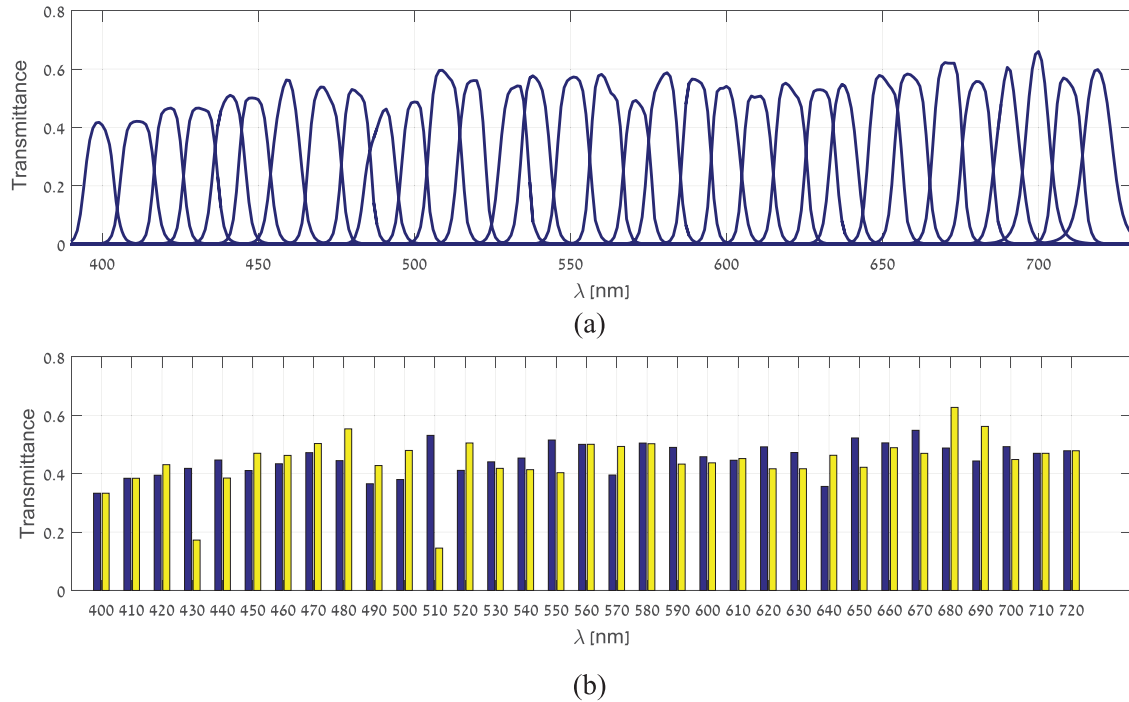


Figure 4. The spectral data for the narrow band-pass filters: (a) nominal spectral transmittance as function of the wavelength, for every filter; (b) averaged within 10 nm wavelength bands transmittance, the left bar– nominal and the right bar – measured.

specifically without the diffuser but with sequentially installed narrow bandpass filters. The pixels within the image of the white patch were spatially averaged for noise reduction. The data from the spectrometer was spectrally averaged down to the 10 nm resolution. Then, the relative spectral sensitivity of the optical system κ_l that participates in Equation (9) was calculated by dividing the data of the image pixels with the data from the spectrometer. At 400, 410, 710 and 720 nm wavelength bands we noticed low SNR due to low spectral power of the iPad screen and used nominal values instead of measured ones.

In the calibration measurements for the monochromatic 1D PSF with a horizontally diffusing 1D diffuser, we displayed a narrow 4-pixels thick white vertical line on the iPad. Then, we imaged it to the image sensor in the dark through sequentially exchanged narrow bandpass filters, which correspond to L wavelength bands. We should note that the white line's width corresponded to a geometrical image width of approximately 2 pixels without a diffuser. Thinner line would have been preferred; however, the chosen width was the minimal to obtain reasonable SNR for the PSF measurements with the diffuser. The measured 1D PSF at different vertical locations of the field of view was provided in this arrangement directly by rows of the image sensor data. The integration time of the image sensor in the PSF measurements varied from one to other wavelength to match effects of chromatic dispersion, variations in the spectrum of the vertical white line, the spectral transmittance of the narrow bandpass filters, quantum efficiency of the image sensor, and the overall spectral sensitivity of the optical system. While the chromatic dispersion, quantum efficiency of the sensor and the spectral sensitivity of the optical system should be embodied in the sensing matrix, the other factors should be compensated. Accordingly, we developed and used the following spectral correction scheme in the PSF measurements, for pixels received from the image sensor:

- (1) Acquire monochromatic image sensor data from the vertical line object through the l th spectral filter.
- (2) Divide the measured pixels values by the integration time at the wavelength band l , relative to minimum integration time.
- (3) Divide the measured pixel values by the corresponding spectrum of the white line object, as obtained by spectrometer before the bandpass filters and downsampled to 10 nm resolution.
- (4) Divide the measured pixel values at each wavelength band by the corresponding bandpass filter's transmittance M_l .

Finally, after the calibration procedure, we get the sensing matrix elements $A_{l',i,l}$ in accordance to Equation (9).

4. Reconstruction of colour data from the monochromatic DD image

For reconstruction of colour coordinates from the DD image, we first reconstructed a spectral cube (27) and then converted from the spectrum at each spatial pixel to the RGB colour coordinates at same pixel, by well-known equations of the CIE 1931 standard (32).

This section presents a set of mathematical equations as follows. Equations (13) and (14) provide the typical CS merit function for the numerical quality of the spectral cube reconstruction; its iterative process is described in Equation (15). Finally, Equations (16) and (17) describe conversion from spectral cube to RGB data of the object, whereas Equations (18)–(20) describe the figure of merit for the reconstruction quality.

The model expressed by Equation (10) shows that the recorded DD image \mathbf{I}' includes a linear mixture of spectral and spatial data of the entire spectral cube \mathbf{I} , as described by sensing matrix \mathbf{A} . The number $N_y \times N_x$ of equations for \mathbf{I}' in Equation (10) is less than the number of unknown variables $N_y \times NL$ in \mathbf{I} . The CS problem consists of the reconstruction of matrix \mathbf{I} in such a way that Equation (10) with a given matrix \mathbf{I}' becomes satisfied with some accuracy. Even though the reconstruction problem seems to be ill-posed and may have an infinite number of solutions, the CS theory (23, 33) resorts to the sparse nature of the 2D digital images to find a sensible solution. The mathematical relation between the spectral cube matrix \mathbf{I} and its respective sparse representation \mathbf{d} can be represented as a linear transform $\mathbf{d} = \mathbf{D}\mathbf{I}$ or inverse transform $\mathbf{I} = \mathbf{\Psi}\mathbf{d}$, with a 'sparsifying' matrix \mathbf{D} , which we implemented as wavelet-framelet transforms (24). Sparsity of an image in the wavelet-frame domain means that \mathbf{d} has relatively small number K of nonzero frame coefficients. The CS theory (23) states that the K -sparse sensible solution \mathbf{d} (and consequently \mathbf{I}) can be reconstructed for a special class of K -sparse matrices $\mathbf{\Theta} = \mathbf{A}\mathbf{\Psi}$ that satisfy a restricted isometry property (RIP) of respective order K (23, 27).

In CS-based reconstruction of sparse representation \mathbf{d} of spectral cube matrix \mathbf{I} from DD image \mathbf{I}' , we look for a solution of Equation (10) that is maximally sparse. Specifically, we resorted to the minimization of a functional

$$\|\mathbf{d}\|_{l_1} + \frac{\mu}{2} \|\mathbf{A}\mathbf{I} - \mathbf{I}'\|_{l_2}^2 + \frac{\chi}{2} \|\mathbf{d} - \mathbf{D}\mathbf{I}\|_{l_2}^2, \quad (13)$$

where μ and χ are Lagrange weight coefficients and the l_1 and l_2 norms are defined as

$$\|\mathbf{d}\|_{l_1} = \sum_{ij} |d_{ij}|, \quad \|\mathbf{d}\|_{l_2} = \sqrt{\sum_{ij} |d_{ij}|^2}. \quad (14)$$

The solution of the minimization problem (Equation (13)) was found by a closed loop of non-adaptive linear projections in the following split Bregman iterative (SBI) process (27, 33–36):

$$\begin{cases} \mathbf{I}^{m+1} = (\mu \mathbf{A}^* \mathbf{A} + \chi \mathbf{E})^{-1} [\mu \mathbf{A}^* (-\mathbf{c}^m) \\ \quad + \chi \mathbf{D}^* (\mathbf{d}^m - \mathbf{b}^m)] \\ \mathbf{d}^{m+1} = \text{shrink}(\mathbf{D} \mathbf{I}^{m+1} + \mathbf{b}^m, \chi^{-1}) \\ \mathbf{b}^{m+1} = \mathbf{b}^m + \delta_b (\mathbf{D} \mathbf{I}^{m+1} - \mathbf{d}^{m+1}) \\ \mathbf{c}^{m+1} = \mathbf{c}^m + \delta_c (\mathbf{A} \mathbf{I}^{m+1} - \mathbf{I}') \end{cases}, \quad (15)$$

where m is the number of the iteration, \mathbf{b}^m and \mathbf{c}^m are intermediate vectors in the execution of the iterations, \mathbf{A}^* denotes a transposed matrix \mathbf{A} , $\delta_b = 1$ and $\delta_c = 1$ are weight parameters, \mathbf{E} is a unit diagonal matrix and the shrink function $\text{shrink}(x, \gamma) = \text{sgn}(x) \max(|x| - \gamma, 0)$ for a threshold γ is applied to each vector component. Here, $\text{sgn}(x)$ is the sign operator, i.e. it equals to $+1$ if x is positive or it equals to -1 if x is strictly negative, and $\max(|x| - \gamma, 0)$ returns the maximal value between $|x| - \gamma$ and 0 . After completion of the iterations (27), we obtain the reconstructed spectral cube \mathbf{I} , with voxels $I_{i,l}^{(j)}$ arranged as a set of vectors with spectral data for every spatial pixel.

In order to transfer from the reconstructed spectral cube \mathbf{I} of dimensions $N_y \times N \times L$ to the required RGB representation of size $N_y \times N \times 3$, the following procedures (37) were applied. We calculated the XYZ colour coordinates at each spatial pixel i, j , $i = \overline{1, N}, j = \overline{1, N_y}$ by resorting to the CIE 1931 XYZ standard observer colour coordinates definition (32), which can be expressed in our notations as

$$\begin{aligned} X_i^{(j)} &= \sum_{l=1}^L I_{i,l}^{(j)} \bar{x}(\lambda_l) \\ Y_i^{(j)} &= \sum_{l=1}^L I_{i,l}^{(j)} \bar{y}(\lambda_l). \\ Z_i^{(j)} &= \sum_{l=1}^L I_{i,l}^{(j)} \bar{z}(\lambda_l) \end{aligned} \quad (16)$$

Here $\bar{x}(\lambda), \bar{y}(\lambda), \bar{z}(\lambda)$ are the CIE's colour matching functions that provide the numerical description of the chromatic response of the standard observer versus wavelength λ of the light (32). Then we scaled XYZ coordinates in Equation (16) to the interval $[0,1]$, by

clipping negative values to 0 and normalizing by the maximal XYZ coordinate value. Subsequent linear conversion from XYZ to standard RGB colour pixel components $C_{i,c}^{(j)}$, denoted with index $c = R, G$ or B was implemented by multiplication over the following constant matrix (38):

$$\begin{bmatrix} C_{i,R}^{(j)} \\ C_{i,G}^{(j)} \\ C_{i,B}^{(j)} \end{bmatrix} = \begin{bmatrix} 3.2406 & -1.5372 & -0.4986 \\ -0.9689 & 1.8758 & 0.0415 \\ 0.0557 & -0.2040 & 1.0570 \end{bmatrix} \begin{bmatrix} X_i^{(j)} \\ Y_i^{(j)} \\ Z_i^{(j)} \end{bmatrix}, \quad (17)$$

with subsequent scaling of the $C_{i,c}^{(j)}$ to the interval $[0,1]$ by clipping their negative values to 0 and values greater than 1 values to 1. We also increased the brightness of the images by multiplying the RGB values by a coefficient $s > 1$. Finally, the reconstructed RGB image comprises $N_y \times N \times 3$ RGB components $\mathbf{C} = (C_{i,c}^{(j)}, i = \overline{1, N}, j = \overline{1, N_y}, c = R, G, B)$.

In order to evaluate the quality and errors in the reconstructed RGB image \mathbf{C} , we compared it to a reference RGB image $\bar{\mathbf{C}}$ of size $N_y \times N \times 3$, whose spectral cube was measured directly with the set of narrow bandpass filters for each of the L wavelengths in the 400–720 nm range. As the reconstructed and the reference RGB images do not necessarily share the same dynamic range, we normalized each of the data arrays $\mathbf{C}, \bar{\mathbf{C}}$ to its maximal values

$$\bar{C}_{\max} = \max_{i,j,c} \bar{C}_{i,c}^{(j)}, \quad C_{\max} = \max_{i,j,c} C_{i,c}^{(j)}, \quad (18)$$

where i, j denotes the spatial pixel and $c = R, G$ or B . Then we expressed the normalized root-mean-square errors (RMSE) of the full RGB image as

$$\text{RMSE} = \left\{ \frac{1}{3NN_y} \sum_{i=1}^N \sum_{j=1}^{N_y} \sum_{c=1}^3 [C_{i,c}^{(j)} / C_{\max} - \bar{C}_{i,c}^{(j)} / \bar{C}_{\max}]^2 \right\}^{0.5}, \quad (19)$$

and calculated the peak signal-to-noise ratio (PSNR) as

$$\text{PSNR} = -20 \log_{10}(\text{RMSE}). \quad (20)$$

For analysis of the separate R, G and B image components we also defined similar quantities $\bar{C}_{\max,c}, C_{\max,c}, \text{RMSE}_c$ and PSNR_c , where $c = R, G, B$, by obvious modification of Equations (18), (19) and (20) in removing maximization and averaging with respect to index c . For even more detailed analysis for the spatial distribution of the RGB image errors, we defined further similar quantities $\bar{C}_{\max,i}^{(j)}, C_{\max,i}^{(j)}, \text{RMSE}_{j,i}$ and $\text{PSNR}_{j,i}$ per spatial pixel, by obvious modification of Equations (18), (19) and (20) in removing maximization and averaging with respect to indices i, j .

5. Results of optical experiment for colour imaging with monochromatic sensor

The concept of our CS-based colour imaging camera was proven in an optical experiment based on the optical arrangement in Figure 2. The hardware included object generator as an iPad screen mounted on the optical bench at a fixed distance of 88 cm in front of the imaging lens, a 5M pixel $N_b = 12$ -bit monochromatic image sensor with Aptina Demo kit (39), a DSL935 Sunex imaging lens, and a wide bandpass spectral filter that is transmitting main region of the 400–700 nm visible range and constructed of Thorlabs' FELH0400 long pass filter cascaded with FESH0700 short pass filter. Specifically, the wide bandpass filter yields a nominal spectral transmittance of at least 91% in most of this range while blocking unwanted light from other regions of the spectrum (i.e. ultra-violet and infrared light), which is not modelled by the sensing matrix but might be detected by the sensor if the wide bandpass filter would be absent. The image sensor had a pixel pitch $\delta_x = \delta_y = 2.20\mu\text{m}$ and 2592×1944 pixels that was enough to include the spread introduced by the diffuser. Even though our generic hardware and software enabled large dimensions, for proof of the concept we actually reconstructed the spectral cube with dimensions $N_y \times N \times L = 256 \times 256 \times 33$ pixels. Front (near first lens surface) position of the 3.2 mm entrance pupil of DSL935 Sunex imaging lens with numerical aperture (NA) of 0.17 enabled proper placing of the diffuser at the pupil. The reference spectral measurements were executed with the Ocean Optics USB4000 spectrometer. The

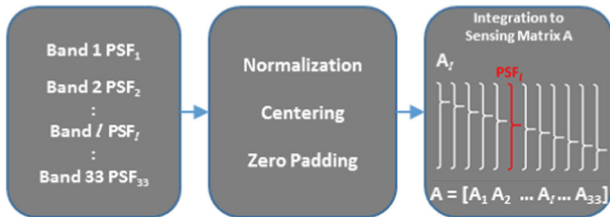


Figure 5. Integration of the PSF data into the sensing matrix **A**.

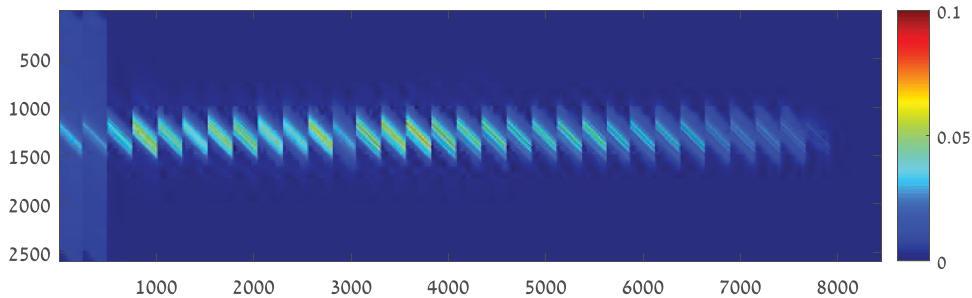


Figure 6. Sensing matrix **A**, built on the base of the calibration measurements. The matrix elements are normalized in the range of $[0,1]$ and are encoded in pseudo-colour in the range of $[0,0.1]$ for display.

1D diffuser with 3.2 mm clear aperture and 400 stripes of $8\mu\text{m}$ width was fabricated at our Nano-centre facilities with a standard 16-depth level binary staircase technology on a 0.5 mm thick, double-side polished fused silica substrate. A special Aluminium holder was used to attach diffusers to the lens housing and conveniently exchange them.

For calibration measurements of the PSF and the sensing matrix following procedure of Section 3, we resorted to the filter wheels with the set of $L = 33$ narrow band-pass spectral filters (Thorlabs FB-XX0-10 Series). The image sensor's integration time was adjusted at each spectral band to keep the peak intensity below 90% of the saturation level. We then subtracted the dark image from measurements and averaged the results for several x, y positions to yield the PSF at each spectral band as a pixel row of the image sensor. The normalized PSF was then centred, padded with zeroes and integrated into the block Toeplitz sensing matrix **A**, as explained in Figure 5. Figure 6 shows the optically measured sensing matrix, consisting of 33 blocks, each matching one wavelength band.

To have firm references for quality evaluation of the CS reconstructed RGB image in our experiments, we conducted direct measurements of the spectral cube for a set of test objects 'Mandrill', 'Colour checker' and 'Peppers', and converted spectral cubes to RGB images. The spectral cube of each test object was directly acquired by imaging, without the diffuser, through a sequentially changed set of L narrow band-pass filters. At each wavelength band l and spatial coordinate j, i , we applied the spectral correction of the measured spectrum by dividing its pixels over narrow bandpass filter's transmittance M_l and the spectral sensitivity value κ_l of the optical system. For a comparison of our spectral-based colour imaging method with regular RGB imaging, we directly acquired RGB images in PNG format by a conventional 5M pixel RGB camera (39) with Bayer CFA. To keep consistency, we used the same Sunex DSL935 imaging lens and placed the wide bandpass filter for the visible range in front of it, as was used for the DD image.

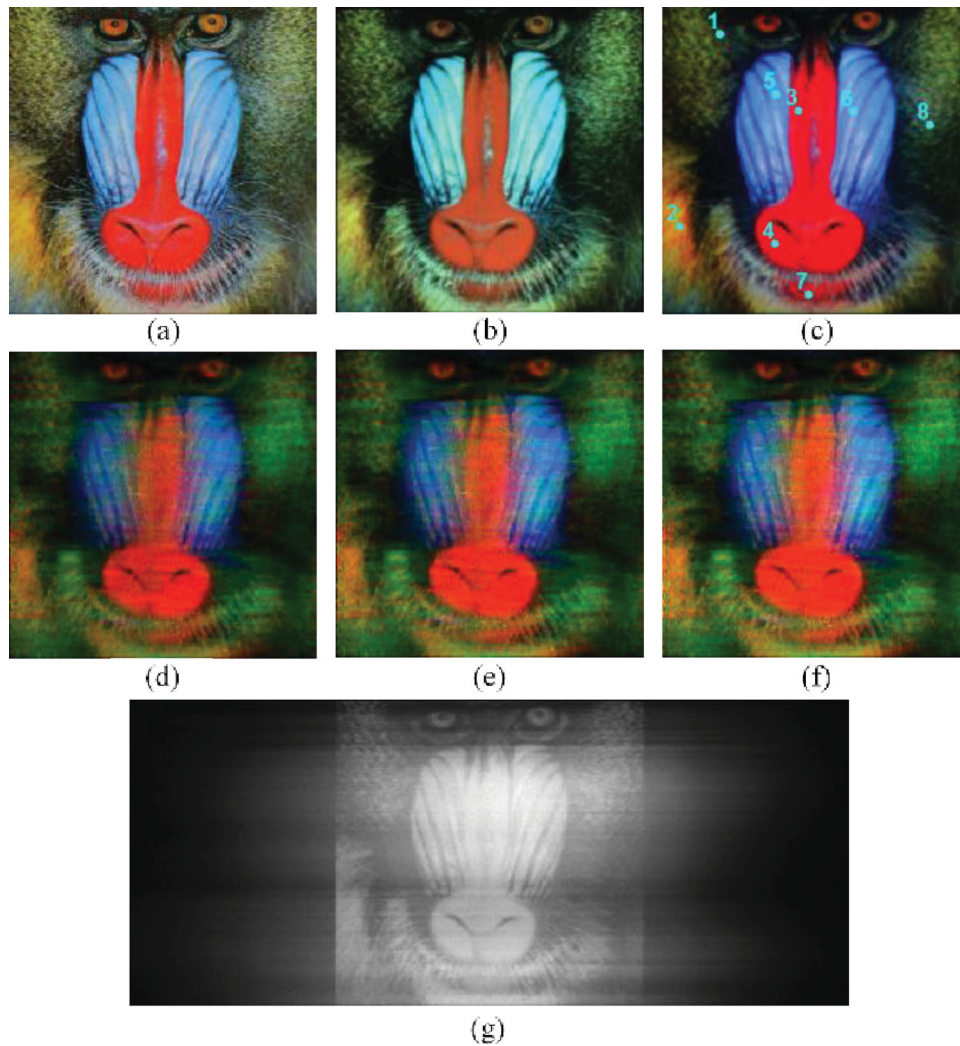


Figure 7. Object 'Mandrill': (a) as displayed on the iPad; (b) directly acquired by the regular RGB sensor; (c) reference calculated from spectral cube measurements with spectral filters; (d)–(f) CS-SSI reconstructed RGB images; (g) DD image.

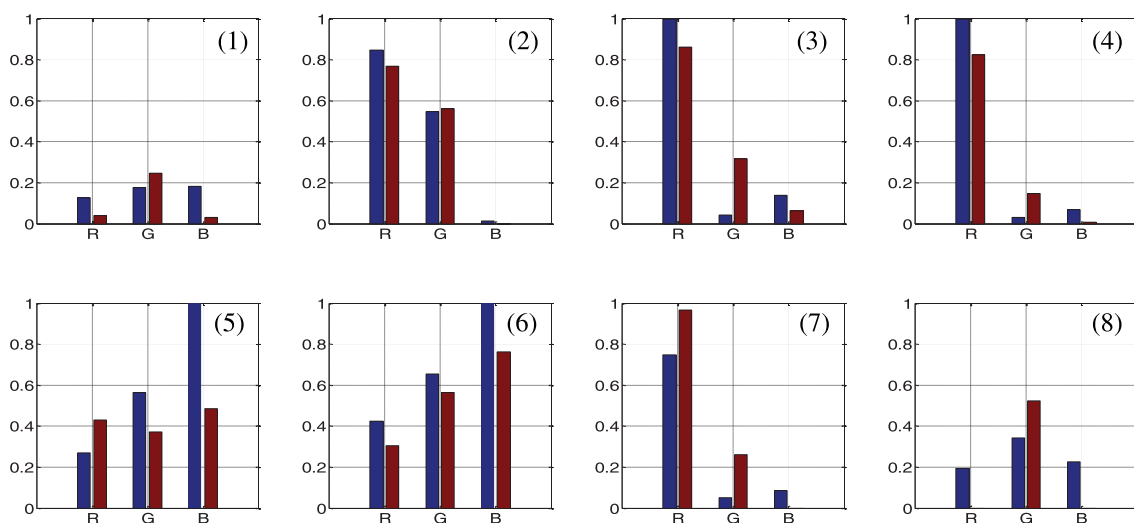


Figure 8. The R, G and B values for the 'Mandrill' at eight sampled spatial locations of Figure 7(c). Blue – reference, red – CS-SSI reconstructed.

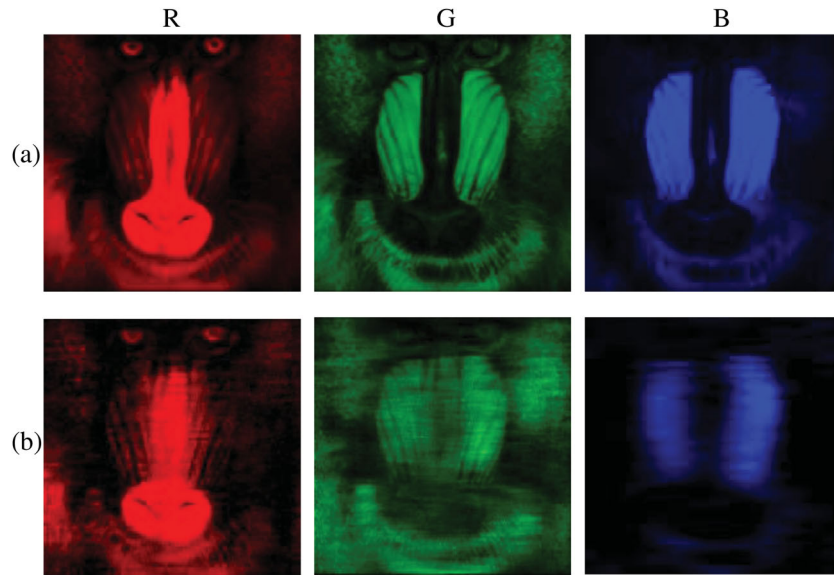


Figure 9. Separated R, G and B images of the 'Mandrill' object: (a) reference, calculated from spectral cube measurements with spectral filters; (b) CS-SSI reconstructed after five SBI applied to DD image.

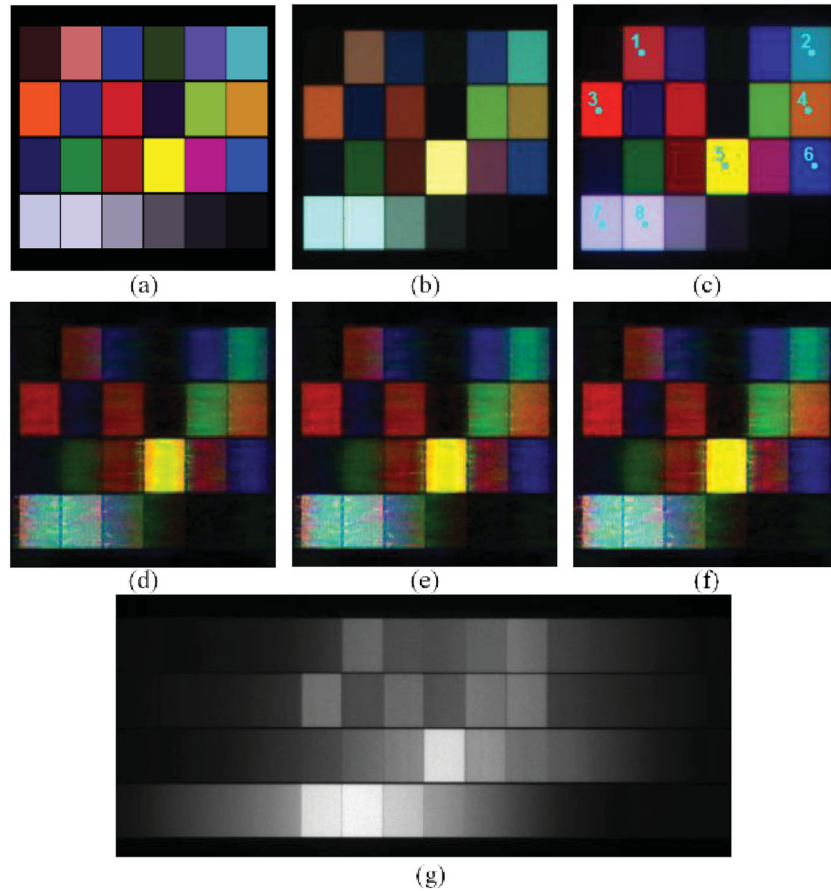


Figure 10. Object 'Colour Checker': (a) as displayed on the iPad; (b) directly acquired by the regular RGB sensor; (c) reference calculated from spectral cube measurements with spectral filters; (d)–(f) CS-SSI reconstructed RGB images; (g) DD image.

In optical bench experiments for snapshot imaging of the coloured objects with the monochromatic image sensor, we acquired several experimental snapshots of DD

images of different objects in the system of Figure 2. The data of the snapshots was digitally pre-processed with a noise reduction filter (40). The digital reconstruction of

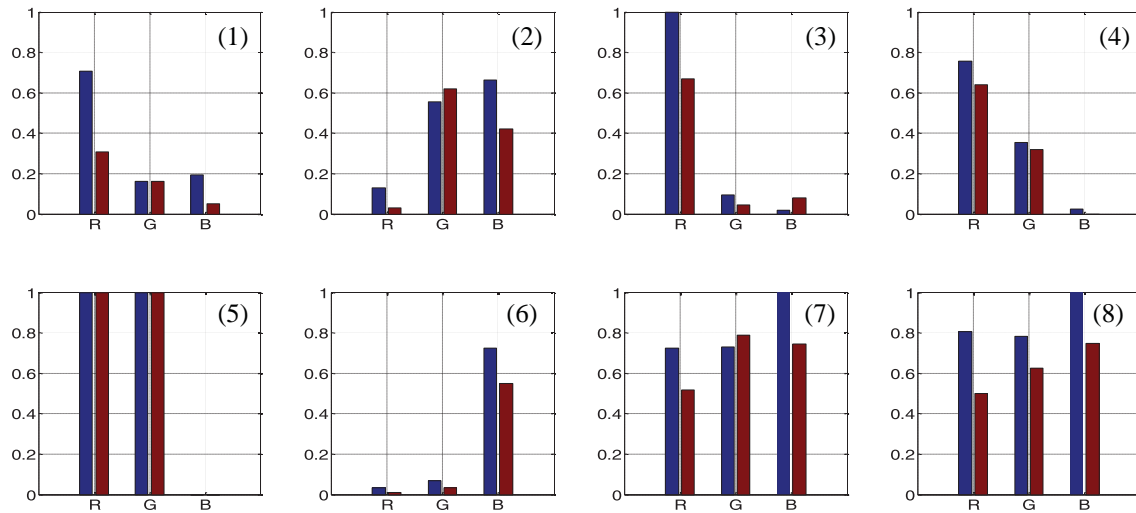


Figure 11. The R, G and B values for the ‘Colour Checker’ at eight sampled spatial locations of Figure 10(c). Blue – reference, red – CS-SSI reconstructed.

the spectral cube was performed using the SBI process with thoroughly optimized parameters μ , χ in Equations (13) and (15). We have also applied spatial median filtering on each of the monochromatic images of the spectral cube after each SB iteration.

Figures 7–16 show experimental results of real optical imaging and subsequent digital processing for obtaining colour RGB images from the monochromatic image sensor. Figures 7, 10, and 13 for the ‘Mandrill’, ‘Colour Checker’ and ‘Peppers’ objects show reference RGB, experimental DD and reconstructed RGB images. Figures 7(a), 10(a), and 13(a) show the original objects as displayed on the iPad, Figures 7(b), 10(b) and 13(b) show directly acquired RGB images, with 13.2, 10.6 and 10.0 ms integration times. Figures 7(c), 10(c) and 13(c) show reference RGB images calculated from spectral cube measurements with the 33 bandpass filters, with a brightness factor of $s = 1.25$. We note that differences between the reference RGB images are related to the differences in the spectral responses of the optical systems and the calculation method of RGB colours using the CIE 1931 standard. Figures 7(d)–(f), 10(d)–(f) and 13(d)–(f) show the RGB images that were CS-SSI reconstructed from the optically recorded experimental data. The CS-SSI reconstruction was based on algorithms of Section 4 with brightness factors of $s = 1$, $s = 1.15$ and $s = 1.25$, respectively. The blurring of the reconstructed B image is likely caused by hazing on some of the blue-region narrow bandpass filters, which were used for the corresponding PSF measurements. Note that some blurring is also observable in the reference B band image, which was calculated from measurements taken with the same set of filters. Additional cause is a low SNR level in the

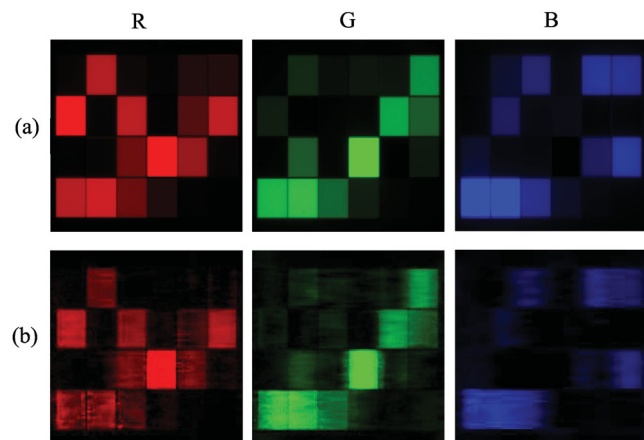


Figure 12. Separated R, G and B images of the ‘Colour Checker’ object. (a) Reference, calculated from spectral cube measurements with spectral filters; (b) CS-SSI reconstructed after four SBI applied to DD image.

PSF measurements at weak spectral regions of the iPad’s screen.

The calculations for PSNR and RMSE between the reference images of Figures 7(c), 10(c), 13(c) and the reconstructed images of Figures 7(f), 10(f), 13(f), RGB images yielded 16.4, 17.1, 19.1 and 0.15, 0.14, 0.11, respectively. Figures 7(g), 10(g) and 13(g) show the DD images acquired in raw PNG format by the monochromatic image sensor with 13.2, 10.6 and 10.0 ms integration times. While dynamic imaging was not tested, we note that these integration times are well suited for video imaging. We emphasize that the RGB images in Figures 7(d)–(f), 10(d)–(f), 13(d)–(f) were obtained with a monochromatic image sensor in a camera equipped

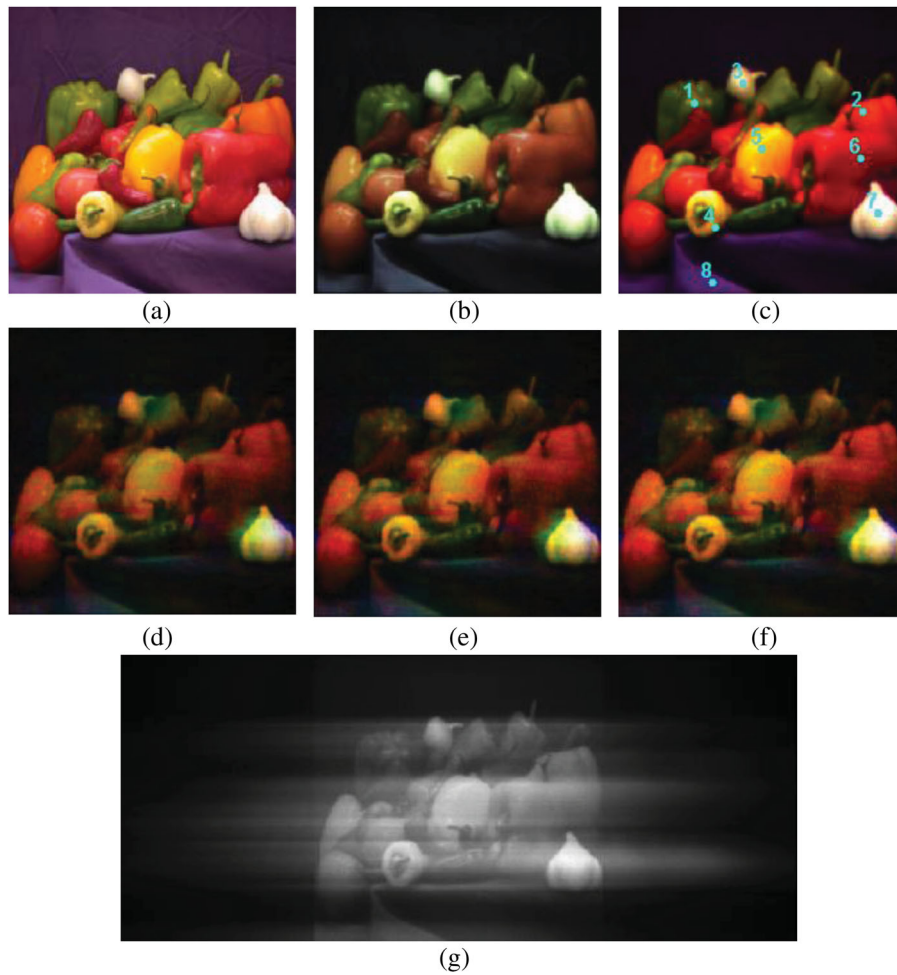


Figure 13. Object ‘Peppers’: (a) as displayed on the iPad; (b) directly acquired by the regular RGB sensor; (c) reference calculated from spectral cube measurements with spectral filters; (d)–(f) CS-SSI reconstructed RGB images; (g) DD image.

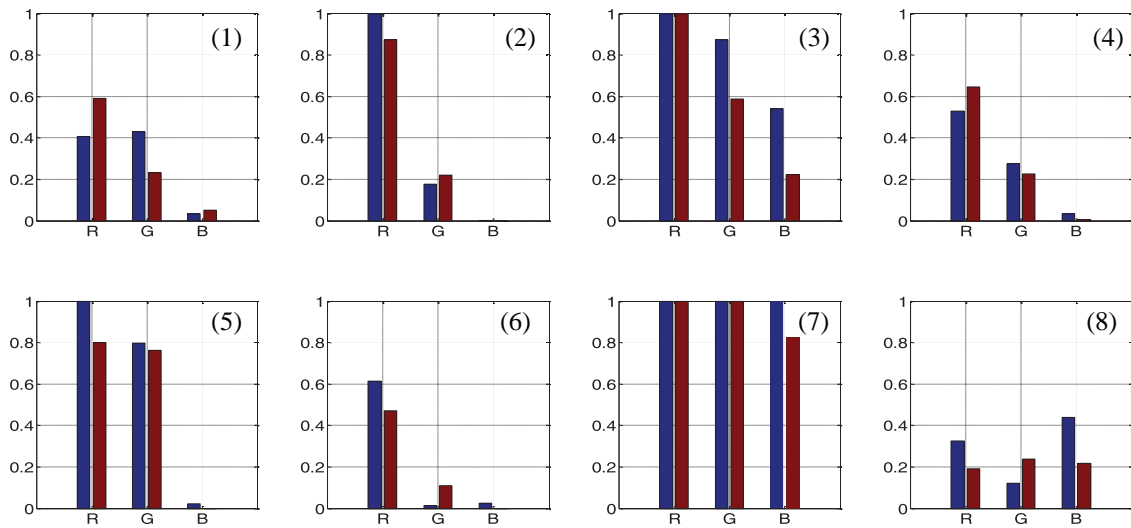


Figure 14. The R, G and B values for the ‘Peppers’ at eight sampled spatial locations of Figure 13(c). Blue – reference, red – CS-SSI reconstructed.

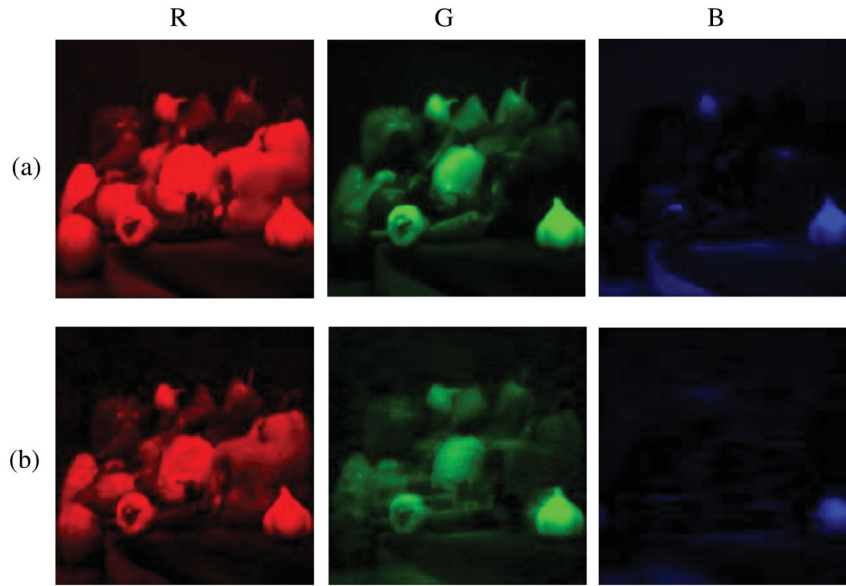


Figure 15. Separated R, G and B images of the ‘Peppers’ object. (a) Reference, calculated from spectral cube measurements with spectral filters; (b) CS-SSI reconstructed after two SBI applied to DD image.

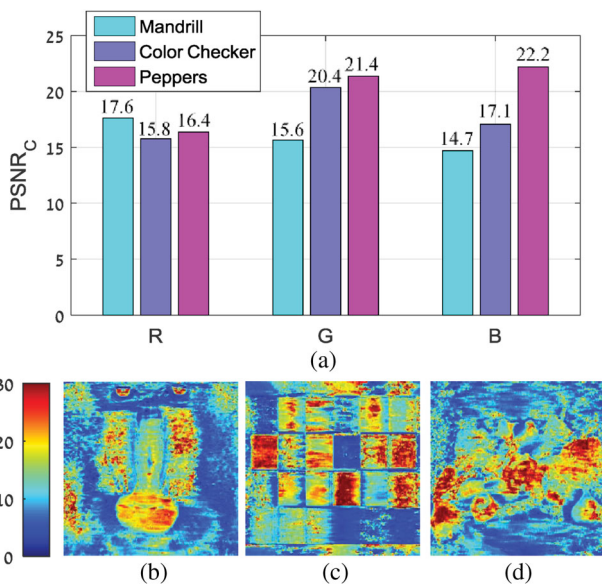


Figure 16. The RGB reconstruction errors for ‘Mandrill’, ‘Colour Checker’ and ‘Peppers’ objects. (a) $PSNR_C$ values of the R, G and B monochromatic images of the ‘Mandrill’, ‘Colour Checker’ and ‘Peppers’ objects; (b)–(d) spatial distribution for $PSNR_{j,i}$ for the same three objects.

with a fully transparent phase-only diffuser. Figures 8, 11 and 14 show a comparison between reference and reconstructed RGB values at 8 sampled spatial coordinates that were marked in Figures 7(c), 10(c) and 13(c). Figures 9, 12 and 15 show the separated R, G and B images of the ‘Mandrill’, ‘Colour Checker’ and ‘Peppers’ objects. Figures 9(a), and 12(a), 15(a) show the reference images and Figures 9(b) and 12(b), 15(b) show the CS-SSI reconstructed RGB images. The $PSNR_C$ ($RMSE_C$) values for

the three objects were following: for Figure 9(b) 5 SBI runs yielded 17.6 (0.13), 15.6 (0.17) and 14.7 (0.18), for Figure 12(b) 4 SBI runs yielded 15.8 (0.16), 20.4 (0.096) and 17.1 (0.14), for Figure 15(b) 2 SBI runs yielded 16.4 (0.15), 21.4 (0.086) and 22.2 (0.078). All values are provided separately for the R, G and B images, respectively. Each iteration took approximately 2 s on Matlab installed on a desktop PC with Windows 7, 64-bit operating system, with 16GB RAM and an Intel i7-3770 processor. Figure 16 shows more details of the reconstruction errors for the ‘Mandrill’, ‘Colour Checker’ and ‘Peppers’ objects. Figure 16(a) shows the $PSNR_C$ values of the R, G and B images of the three objects, while Figures 16(b)–(d) show the spatial distribution $PSNR_{j,i}$ for the same three objects. To summarize, Figures 7–16 reveal satisfactory visual quality and PSNR levels of the RGB images obtained from the monochromatic image sensor. Artefacts in the reconstructed RGB images are most probably linked to some mis-calibrations of the sensing matrix, the presence of actual system noise and quantization of the sensor and the sensitivity of the reconstruction algorithm to these factors. Quantitative evaluation for spatial resolution in the reconstructed images is due to be performed in future experiments.

6. Light throughput of the RGB camera with monochromatic image sensor

Light throughput is one of the most important and competitive features of the proposed colour imaging with a monochromatic image sensor. In order to evaluate the light throughput of our method, we shot images of white,

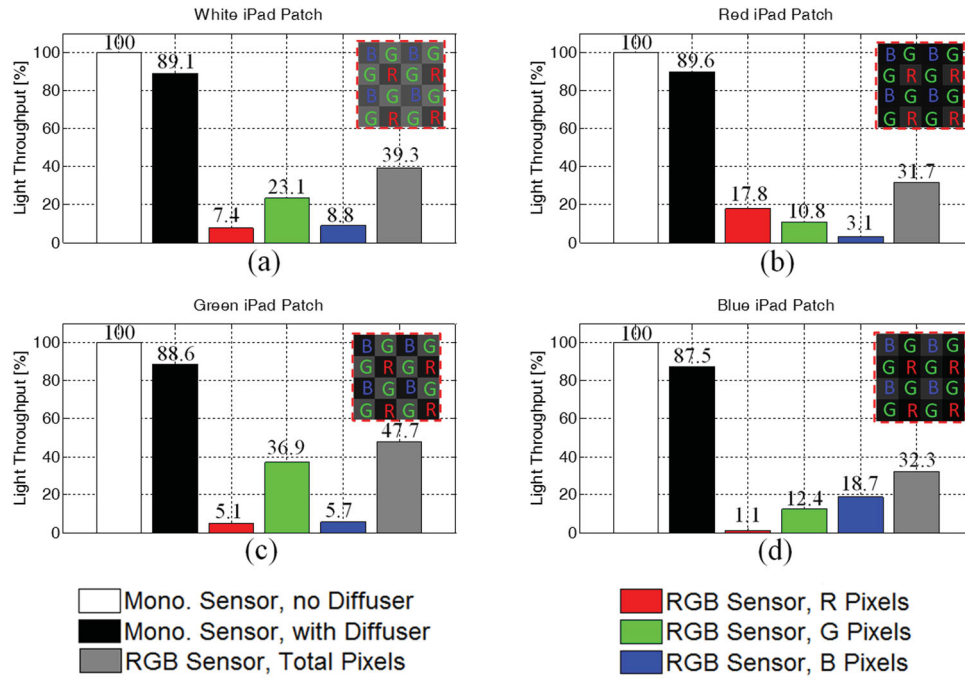


Figure 17. Light throughput comparison results between our camera and reference CFA RGB camera, based on raw PNG-format data. iPad objects were patches of different colours (a) white, (b) red, (c) green and (d) blue. Insets show fragments of the raw images from the RGB sensor.

red, green and blue uniform object patches from the iPad screen and compared results of our method with regular RGB imaging. Each patch was shot in three different hardware configurations: (i) by the monochromatic camera with all ‘white’ pixels and without the diffuser, when the image of each patch corresponded to 256×256 pixels on the sensor plane; (ii) by the monochromatic camera with the diffuser; (iii) by the regular 5Mp RGB camera with Bayer CFA. The same imaging lens and wide bandpass spectral filter for the visible range were used in all of the measurement modes. The integration time in the monochromatic image sensor was set to 2.6 ms, which satisfied a peak intensity of 90% of the saturation intensity level in the case without the diffuser. The integration time was identical and equalled to 2.6 ms for the monochromatic camera measurements (without and with the diffuser) and for the colour camera measurements (without the diffuser). For noise reduction, each image was obtained by sequential averaging of 25 frames. The images were obtained in raw PNG format, to avoid any corrections by the built-in graphic processor of the camera. We also obtained and subtracted corresponding dark images from the measurements.

Figure 17 shows light throughput percentage bars for each measurement mode and each of the colours of patch object. At the Bayer CFA camera, the nonzero pixels that do not match the R, G and B objects characterize spectral ‘cross-talks’ between the RGB primaries of the sensor

and the iPad screen. The total light in arbitrary units was calculated by summing the camera pixels, i.e. light intensities values. For the monochromatic camera without the diffuser, calculation of the flux was performed within 256×256 pixels. For the monochromatic camera with the diffuser, flux calculation was extended to 256×2592 pixels of the DD image. For the RGB camera, flux calculation was applied separately for each of the R, G and B pixel groups within boundaries of the image of the patch object, i.e. 128×128 pixels for each of R and B images and $2 \times 128 \times 128$ pixels for the G image.

The ratio of light flux in different configurations was referenced to the flux obtained by the monochromatic camera without the diffuser. Figure 17(a) shows that the light throughput of our method for the white patch object is approximately 89% from that of the monochromatic camera with all ‘white’ pixels. This value is significantly higher than the 39% total light throughput of the RGB camera with Bayer CFA, calculated for all R, G and B pixels altogether. Figure 17(b)–(d) show that the light throughput of our method for the colour objects is between 87.5% and 89.6% from that of the monochromatic camera with all ‘white’ pixels. This throughput is significantly higher than the corresponding 17.8%, 36.9% and 18.7% values of the Bayer CFA sensor. Therefore, our method provides more than double gain in the light throughput, compared to an equivalent regular RGB camera equipped with a conventional Bayer CFA. Such

gains were expected, because a CFA in a regular RGB camera absorbs roughly two-third of the incident light in either of the R, G or B filters, while our suggested method makes use of a highly efficient transparent phase-only diffuser.

7. Discussion and conclusions

We experimentally proved the feasibility of colour imaging with a monochromatic image sensor and a pupil domain phase-only static diffuser. In our approach, the light transmittance throughput is more than twice higher than with customarily used light absorbing RGB Bayer colour filter arrays. The experimental results that are presented in this paper exhibit improved quality of the reconstructed RGB images in respect to our published results in (27). The improvement is explained by better calibration of the sensing matrix and thorough optimization of parameters in the reconstruction algorithm.

The key element of our optical system is a diffuser designed to create a randomized sensing matrix that is evaluated directly from calibration measurements of the PSF. The diffuser can be produced by routine diffractive optics technology in required quantities, including those of consumer-market mobile devices. The diffuser may be an embedded integral part of a dedicated monochromatic digital camera of a mobile device or alternatively serve as an external patch on the window of a digital camera. Future research will focus on investigating new diffuser designs which may lead to improved results by better fulfilling the RIP condition towards reducing the correlation between the PSFs of the spectral bands.

The use of a monochromatic sensor instead of a regular mosaic colour sensor increases the amount of the captured light and therefore the sensitivity of the camera, which delivers significant advantages for low light imaging applications.

Our method relies substantially on spatial and spectral mixing of the 2D light field at the image sensor and subsequent reconstruction of the spatial and colour data with CS-based algorithms. The latter is achieved by proper use of the sparsity property, naturally attributed to photographic images. We experimentally demonstrated the feasibility of reconstructing RGB images through SSI and linear iterative process of split Bregman iterations. The developed spectral-wise based colour imaging algorithms can be implemented in the firmware of digital cameras.

To conclude, we propose that the commonly used Bayer colour filter array at an image sensor can be substituted with a transparent, phase-only diffuser at the pupil, thus improving the light throughput of the optical system.

While high light throughput is already achieved in our method, spatial resolution, signal-to-noise ratio and colour rendering quality still have to be improved in further research. For quality improvement in further research, we foresee optimization of the pupil diffuser, more precise calibration of the sensing matrix of the imaging system at different object distances and light power levels, development of efficient compressive sensing algorithms directly in space of colour coordinates and extended experimenting with real objects out of the lab.

Disclosure statement

No potential conflict of interest was reported by the authors.

Funding

This research was partially supported by Israeli Ministry of Science Technology and Space [grant numbers 3-10416 and 3-13601].

ORCID

Jonathan Hauser  <http://orcid.org/0000-0003-0767-0771>

References

- (1) Nassimbene, E.G. Color Video Record and Playback System. US Patent 3,529,080, September 15, 1970.
- (2) Sampell, J. White Light Enhanced Color Field Sequential Projection. US Patent 5,233,385, August 3, 1993.
- (3) Šolc, I. Chain Bi-refringent Filters. *Czechoslovakij fiziceskij zurnal*. 1959, 9 (2), 237–249.
- (4) Liu, C.-K.; Cheng, K.-T.; Fuh, A.Y.-G. Designs of High Color Purity RGB Color Filter for Liquid Crystal Displays Applications Using Fabry-Perot Etalons. *J. Disp. Technol.* 2012, 8, 174–178.
- (5) Miller, P.J.; Hoyt, C.C. Multispectral Imaging with a Liquid Crystal Tunable Filter. *SPIE*. 1995. doi:10.1117/12.198889.
- (6) Raz, A.; Mendlovic, D. Sequential Filtering for Color Image Acquisition. *Opt. Express*. 2014, 22, 26878–26883.
- (7) Bayer, B. Color Imaging Array. US Patent 3,971,065, July 20, 1976.
- (8) Honda, H.; Iida, Y.; Itoh, G.; Egawa, Y.; Seki, H. A Novel Bayer-like WRGB Color Filter Array for CMOS Image Sensors. *SPIE*. 2007, 6492, 64921J.1–64921J.10.
- (9) Chakrabarti, A.; Freeman, W.T.; Zickler, T. Rethinking Color Cameras. *2014 IEEE International Conference on Computational Photography (ICCP)*, Santa Clara, California, USA, 2014.
- (10) Lyon, R.F.; Merrill, R.B.; Foveon Inc. Vertical Color Filter Sensor Group Array that Emulates a Pattern of Single-layer Sensors with Efficient Use of Each Sensor Group's Sensors. US Patent 6,998,660 B2, February 14, 2006.
- (11) <http://www.jai.com/en/products/multi-imager/colour-areascancameras> (accessed March 26, 2018).
- (12) Brady, D.J. *Optical Imaging and Spectroscopy*, Wiley-Interscience: Duke University, Durham, North Carolina, 2009.

- (13) Garini, Y.; Young, I.T.; McNamara, G. Spectral Imaging: Principles and Applications. *Cytom. A.* **2006**, *69A*, 735–747.
- (14) Uhr, J.W.; Huebschman, M.L.; Frenkel, E.P.; Lane, N.L.; Ashfaq, R.; Liu, H.; Rana, D.R.; Cheng, L.; Lin, A.T.; Hughes, G.A.; Zhang, X.J.; Garner, H.R. Molecular Profiling of Individual Tumor Cells by Hyperspectral Microscopic Imaging. *Transl. Res.* **2012**, *159*, 366–375.
- (15) Long, R.L.; Walsh, K.B.; Greensill, C.V. Sugar ‘Imaging’ of Fruit Using a Low Cost Charge-Coupled Device Camera. *J. Near Infrared Spectrosc.* **2005**, *13*, 177–186.
- (16) Lang, H. Advances in Multispectral and Hyperspectral Imaging for Archaeology and art Conservation. *Appl. Phys.* **2012**, *106*, 309–323.
- (17) Foster, D.H.; Amano, K.; Nascimento, S.M.C.; Foster, M.J. Frequency of Metamerism in Natural Scenes. *J. Opt. Soc. Am. A.* **2006**, *23*, 2359–2372.
- (18) Yuan, X.; Tsai, T.-H.; Zhu, R.; Lull, P.; Brady, D.J.; Carin, L. Compressive Hyperspectral Imaging with Side Information. *IEEE J. Sel. Top. Signal Process.* **2015**, *9*, 964–976.
- (19) Gao, L.; Kester, R.T.; Hagen, N.; Tkaczyk, T.S. Snapshot Image Mapping Spectrometer (IMS) with High Sampling Density for Hyperspectral Microscopy. *Opt. Express.* **2010**, *18*, 14330–14344.
- (20) Descour, M.; Dereniak, E.L. Computed-tomography Imaging Spectrometer: Experimental Calibration and Reconstruction Results. *Appl. Opt.* **1995**, *34*, 4817–4826.
- (21) Gorman, A.; Fletcher-Holmes, D.W.; Harvey, A.R. Generalization of the Lyot Filter and Its Application to Snapshot Spectral Imaging. *Opt. Express.* **2010**, *18*, 5602–5608.
- (22) Wagadarikar, A.; John, R.; Willett, R.; Brady, D. Single Disperser Design for Coded Aperture Snapshot Spectral Imaging. *Appl. Opt.* **2008**, *47*, B44–B51.
- (23) Donoho, D.L. Compressed Sensing. *IEEE Trans. Inform. Theory* **2006**, *52*, 1289–1306.
- (24) Averbuch, A.; Neittaanmäki, P.; Zheludev, V. *Spline and Spline Wavelet Methods with Applications to Signal and Image Processing*, Vol. 1. Periodic splines, Springer: Tel Aviv University, Tel Aviv and University of Jyväskylä, Jyväskylä, 2014.
- (25) Candès, E.J.; Romberg, J.K.; Tao, T. Stable Signal Recovery from Incomplete and Inaccurate Measurements. *Commun. Pure Appl. Math.* **2006**, *59*, 1207–1223.
- (26) Arguello, H.; Arce, G.R. Restricted Isometry Property in Coded Aperture Compressive Spectral Imaging. *IEEE Statistical Signal Processing Workshop (SSP)*, Ann Arbor, Michigan, USA, 2012.
- (27) Golub, M.A.; Averbuch, A.; Nathan, M.; Zheludev, V.A.; Hauser, J.; Gurevitch, S.; Malinsky, R.; Kagan, A. Compressed Sensing Snapshot Spectral Imaging by a Regular Digital Camera with an Added Optical Diffuser. *Appl. Opt.* **2016**, *55* (3), 432–443.
- (28) Stern, A. *Optical Compressive Sensing*, CRC Press: Ben-Gurion University of the Negev, Beer-Sheva, 2016.
- (29) Wang, P.; Menon, R. Ultra-high-sensitivity Color Imaging via a Transparent Diffractive-filter Array and Computational Optics. *Optica.* **2015**, *2*, 933–939.
- (30) Wang, P.; Menon, R. Computational Multispectral Video Imaging [Invited]. *J. Opt. Soc. Am. A.* **2018**, *35*, 189–199.
- (31) Sahoo, S.K.; Tang, D.; Dang, C. Single-shot Multispectral Imaging with a Monochromatic Camera. *Optica* **2017**, *4*, 1209–1213.
- (32) Smith, T.; Guild, J. The C.I.E. Colourimetric Standards and their Use. *Trans. Opt. Soc.* **1932**, *33* (3), 73–134. doi:10.1088/1475-4878/33/3/301.
- (33) Shen, Z. Wavelet Frames and Image Restorations. In *Proceedings of the International Congress of Mathematicians*; Bhatia, R., Ed., Vol. IV; Hindustan Book Agency: New Delhi, 2010; pp 2834–2863.
- (34) Goldstein, T.; Osher, S. The Split Bregman Method for L1-Regularized Problems. *SIAM J. Imaging Sci.* **2009**, *2*, 323–343.
- (35) Cai, J.-F.; Osher, S.; Shen, Z. Split Bregman Methods and Frame Based Image Restoration. *Multiscale Model. Simul.* **2010**, *8*, 337–369.
- (36) Averbuch, A.Z.; Zheludev, V.A.; Cohen, T. Interpolatory Frames in Signal Space. *IEEE Trans. Sign. Proc.* **2006**, *54*, 2126–2139.
- (37) Foster, D.H. http://personalpages.manchester.ac.uk/staff/d.h.foster/Tutorial_HSI2RGB/Tutorial_HSI2RGB.html (accessed July 10, 2017).
- (38) International Electrotechnical Commission (IEC) 61966-2-1:1999. Multimedia Systems and Equipment – Colour Measurement and Management – Part 2-1: Colour Management – Default RGB Colour Space – sRGB. October 1999.
- (39) Aptina Imaging Demo kits. <https://www.onsemi.com/PowerSolutions/product.do?id=MT9P031> (accessed July 30, 2017).
- (40) Maggioni, M.; Sánchez-Monge, E.; Foi, A.; Danielyan, A.; Dabov, K.; Katkovnik, V.; Egiazarian, K. Image and Video Denoising by Sparse 3D Transform-domain Collaborative Filtering, <http://www.cs.tut.fi/foi/GCF-BM3D/> (accessed January 15, 2019), 2007.